High-efficiency degenerate four-wave mixing in triply resonant nanobeam cavities

Zin Lin,[1,][*] Thomas Alcorn,[2] Marko Loncar,[1] Steven G. Johnson,[2] and Alejandro W. Rodriguez[3]

[1]*School of Engineering and Applied Sciences, Harvard University, Cambridge, Massachusetts 02138, USA*
[2]*Department of Mathematics, Massachusetts Institute of Technology, Cambridge, Massachusetts 02139, USA*
[3]*Department of Electrical Engineering, Princeton University, Princeton, New Jersey 08544, USA*

Using a combination of temporal coupled-mode theory and nonlinear finite-difference time-domain (FDTD) simulations, we study the nonlinear dynamics of all-resonant four-wave mixing processes and demonstrate the possibility of achieving high-efficiency limit cycles and steady states that lead to ≈100% depletion of the incident light at low input (critical) powers. Our analysis extends previous predictions to capture important effects associated with losses, self- and cross-phase modulation, and imperfect frequency matching (detuning) of the cavity frequencies. We find that maximum steady-state conversion is hypersensitive to frequency mismatch, resulting in high-efficiency limit cycles that arise from the presence of a homoclinic bifurcation in the solution phase space, but that a judicious choice of incident frequencies and input powers, in conjuction with self-phase and cross-phase modulation, can restore high-efficiency steady-state conversion even for large frequency mismatch. Assuming operation in the telecom range, we predict close to perfect quantum efficiencies at reasonably low ∼50 mW input powers in silicon micrometer-scale PhC nanobeam cavities.

PACS number(s): 42.65.Ky, 42.60.Da, 42.65.Sf, 42.65.Jx

I. INTRODUCTION

Optical nonlinearities play an important role in numerous photonic applications, including frequency conversion and modulation [1–7], light amplification and lasing [1,8–10], beam focusing [1,11], phase conjugation [1,12], signal processing [13,14], and optical isolation [15,16]. Recent developments in nanofabrication are enabling fabrication of nanophotonic structures, e.g., waveguides and cavities that confine light over long times and small volumes [17–21], minimizing the power requirements of nonlinear devices [22,23] and paving the way for novel on-chip applications based on all-optical nonlinear effects [18,24–33]. In addition to greatly enhancing light-matter interactions, the use of cavities can also lead to qualitatively rich dynamical phenomena, including multistability and limit cycles [34–40]. In this paper, we explore realistic microcavity designs that enable highly efficient degenerate four-wave mixing (DFWM) beyond the undepleted pump regime. In particular, we extend the results of our previous work [41], which focused on the theoretical description of DFWM in triply resonant systems via the temporal coupled-mode theory (TCMT) framework, to account for various realistic and important effects, including linear losses, self-phase and cross-phase modulation, and frequency mismatch. Specifically, we consider the nonlinear process depicted in Fig. 1, in which incident light at two nearby frequencies, a pump ω_0 and signal $\omega_m = \omega_0 - \Delta\omega$ photon, is up-converted into output light at another nearby frequency, an idler $\omega_p = \omega_0 + \Delta\omega$ photon, inside a triply resonant photonic crystal nanobeam cavity (depicted schematically in Fig. 2). We demonstrate that 100% conversion efficiency (complete depletion of the pump power) can be achieved at a critical power and that detrimental effects associated with self-phase and cross-phase modulation can be overcome by appropriate

tuning of the cavity resonances. Surprisingly, we find that critical solutions associated with maximal frequency conversion are ultrasensitive to frequency mismatch (deviations from perfect frequency matching resulting from fabrication imperfections), but that there exist other robust, dynamical states (e.g., "depleted" states and limit cycles) that, when properly excited, can result in high conversion efficiencies at reasonable pump powers. We demonstrate realistic designs based on PhC nanobeam cavities that yield 100% conversion efficiencies at ∼50 mW pump powers and over broad bandwidths (modal lifetimes $Q \sim 1000$ s). Although our cavity designs and power requirements are obtained using the TCMT framework, we validate these predictions by checking them against rigorous, nonlinear finite-difference time-domain (FDTD) simulations.

Although chip-scale nonlinear frequency conversion has been a topic of interest for decades [33], most theoretical and experimental works have been primarily focused on large-etalon and singly resonant systems exhibiting either large footprints and small bandwidths [25,26,42,43], or low conversion efficiencies (the undepleted pump regime) [22,44–46]. These include studies of $\chi^{(2)}$ processes such as second harmonic generation [26,47–49], sum and difference frequency generation [50], and optical parametric amplification [27,28,51], as well as $\chi^{(3)}$ processes such as third harmonic generation [47,52], four-wave mixing [53–55], and optical parametric oscillators [22,56–58]. Studies that go beyond the undepleted regime and/or employ resonant cavities reveal complex nonlinear dynamics in addition to high-efficiency conversion [23,37–39,41,59,60], but have primarily focused on ring-resonator geometries due to their simplicity and high degree of tunability [60]. Significant efforts are underway to explore similar functionality in wavelength-scale photonic components (e.g., photonic crystal cavities) [49,50], although high-efficiency conversion has yet to be experimentally demonstrated. Photonic crystal nanobeam cavities not only offer a high degree of tunability, but also mitigate
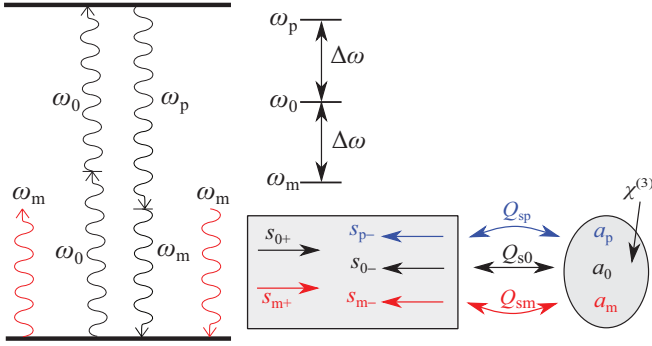
---

*zlin@seas.harvard.edu

FIG. 1. (Color online) Schematic diagram of a degenerate four-wave mixing process in which a pump photon at frequency ω_0 and a signal photon at frequency $\omega_m = \omega_0 - \Delta\omega$ are converted into an idler photon at $\omega_p = \omega_0 + \Delta\omega$ and an additional signal photon at ω_m, inside of a triply resonant $\chi^{(3)}$ nonlinear cavity. The cavity supports three resonant modes with frequencies ω_{ck}, lifetimes Q_k, and modal amplitudes a_k, which are coupled to a waveguide supporting propagating modes at the incident or output frequencies ω_k, with coupling lifetimes Q_{sk}. The incident and output powers associated with the kth mode are given by $|s_{k+}|^2$ and $|s_{k-}|^2$.

the well-known volume and bandwidth tradeoffs associated with ring resonators [61], yielding minimal device footprint and on-chip integrability [62,63], in addition to high-quality factors [21,64–67].

In what follows, we investigate the conditions and design criteria needed to achieve high-efficiency DFWM in realistic nanobeam cavities. Our paper is divided into two primary sections. In Sec. II, we revisit the TCMT framework introduced in Ref. [41], and extend it to include additional effects arising from cavity losses (Sec. II A), self-phase and cross-phase
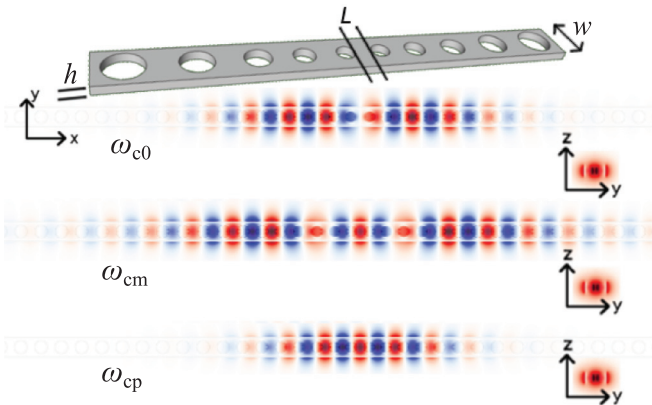

FIG. 2. (Color online) Schematic of 3D triply resonant cavity design involving a PhC nanobeam of refractive index $n = 3.4$, width $w = a$, and height $h = 0.51a$, and linearly tapered air holes, as described in the text. The central cavity length $L \approx 0.4a$ and number of taper segments are chosen so as to fine-tune the relative frequency spacing and lifetimes of the modes. Also shown are the E_y electric-field components of three TE-like modes with fundamental TE00 transverse profiles, and with frequencies $\omega_{c0} = 0.2848(\frac{2\pi c}{a})$, $\omega_{cm} = 0.2801(\frac{2\pi c}{a})$, and $\omega_{cp} = 0.2895(\frac{2\pi c}{a})$. Radiation lifetimes are found to be $Q_0^{\text{rad}} = 10^6, Q_m^{\text{rad}} = 3 \times 10^4$, and $Q_p^{\text{rad}} = 2 \times 10^4$.

modulation (Sec. II B), and frequency mismatch (Sec. II C). In Sec. III, we consider specific designs, starting with a simple two-dimensional (2D) design (Sec. III A) and concluding with a more realistic three-dimensional (3D) design suitable for experimental realization (Sec. III B). The predictions of our TCMT are checked and validated in the 2D case against exact nonlinear FDTD simulations.

II. ANALYSIS VIA TEMPORAL COUPLED-MODE THEORY

To obtain accurate predictions for realistic designs, we extend the TCMT predictions found in Ref. [41] to include important effects associated with the presence of losses, self-phase and cross-phase modulation, and imperfect frequency matching. We consider the DFWM process depicted in Fig. 1, in which incident light from some input or output channel (e.g., a waveguide) at frequencies ω_0 and ω_m is converted to output light at a different frequency $\omega_p = 2\omega_0 - \omega_m$ inside a triply resonant $\chi^{(3)}$ cavity. The fundamental assumption of TCMT (accurate for weak nonlinearities) is that any such system, regardless of geometry, can be accurately described by a few sets of geometry-specific parameters [41]. These include the frequencies ω_{ck} and corresponding lifetimes τ_k (or quality factors $Q_k = \omega_{ck}\tau_k/2$) of the cavity modes, as well as nonlinear coupling coefficients $\alpha_{kk'}$ and β_k, determined by overlap integrals between the cavity modes (and often derived from perturbation theory [23]). Note that, in general, the total decay rate $(1/\tau_k)$ of the modes consist of decay into the input or output channel $(1/\tau_{sk})$, as well as external (e.g., absorption or radiation) losses with decay rate $1/\tau_{ek}$, so that $1/\tau_k = 1/\tau_{sk} + 1/\tau_{ek}$. Letting a_k denote the time-dependent complex amplitude of the kth cavity mode (normalized so that $|a_k|^2$ is the electromagnetic energy stored in this mode), and letting $s_{k\pm}$ denote the time-dependent amplitude of the incident (+) and outgoing (−) light (normalized so that $|s_{k\pm}|^2$ is the power at the incident or output frequency ω_k), it follows that the field amplitudes are determined by the following set of coupled ordinary differential equations [23]:

$$\frac{da_0}{dt} = i\omega_{c0}(1 - \alpha_{00}|a_0|^2 - \alpha_{0m}|a_m|^2 - \alpha_{0p}|a_p|^2)a_0$$

$$- \frac{a_0}{\tau_0} - i\omega_{c0}\beta_0 a_0^* a_m a_p + \sqrt{\frac{2}{\tau_{s0}}}s_{0+}, \quad (1)$$

$$\frac{da_m}{dt} = i\omega_{cm}(1 - \alpha_{m0}|a_0|^2 - \alpha_{mm}|a_m|^2 - \alpha_{mp}|a_p|^2)a_m$$

$$- \frac{a_m}{\tau_m} - i\omega_{cm}\beta_m a_0^2 a_p^* + \sqrt{\frac{2}{\tau_{sm}}}s_{m+}, \quad (2)$$

$$\frac{da_p}{dt} = i\omega_{cp}(1 - \alpha_{p0}|a_0|^2 - \alpha_{pm}|a_m|^2 - \alpha_{pp}|a_p|^2)a_p$$

$$- \frac{a_p}{\tau_p} - i\omega_{cp}\beta_p a_0^2 a_m^*, \quad (3)$$

$$s_{0-} = \sqrt{\frac{2}{\tau_{s0}}}a_0 - s_{0+}, \quad s_{m-} = \sqrt{\frac{2}{\tau_{sm}}}a_m - s_{m+},$$

$$s_{p-} = \sqrt{\frac{2}{\tau_{sp}}}a_p, \quad (4)$$

where the nonlinear coupling coefficients [41]

$$\alpha_{kk} = \frac{1}{8} \frac{\int d^3\mathbf{x}\epsilon_0\chi^{(3)}[2|\mathbf{E}_k \cdot \mathbf{E}_k^*|^2 + |\mathbf{E}_k \cdot \mathbf{E}_k|^2]}{\left(\int d^3\mathbf{x}\epsilon|\mathbf{E}_k|^2\right)^2}, \quad (5)$$

$$\alpha_{kk'} = \frac{1}{4} \frac{\int d^3\mathbf{x}\epsilon_0\chi^{(3)}[|\mathbf{E}_k \cdot \mathbf{E}_{k'}^*|^2 + |\mathbf{E}_k \cdot \mathbf{E}_{k'}|^2 + |\mathbf{E}_k|^2|\mathbf{E}_{k'}|^2]}{\left(\int d^3\mathbf{x}\epsilon|\mathbf{E}_k|^2\right)\left(\int d^3\mathbf{x}\epsilon|\mathbf{E}_{k'}|^2\right)}, \quad (6)$$

$$\alpha_{kk'} = \alpha_{k'k}, \quad (7)$$

$$\beta_0 = \frac{1}{4} \frac{\int d^3\mathbf{x}\epsilon_0\chi^{(3)}[(\mathbf{E}_0^* \cdot \mathbf{E}_0^*)(\mathbf{E}_m \cdot \mathbf{E}_p) + 2(\mathbf{E}_0^* \cdot \mathbf{E}_m)(\mathbf{E}_0^* \cdot \mathbf{E}_p)]}{\left(\int d^3\mathbf{x}\epsilon|\mathbf{E}_0|^2\right)\left(\int d^3\mathbf{x}\epsilon|\mathbf{E}_m|^2\right)^{1/2}\left(\int d^3\mathbf{x}\epsilon|\mathbf{E}_p|^2\right)^{1/2}}, \quad (8)$$

$$\beta_m = \beta_p = \beta_0^*/2, \quad (9)$$

express the strength of the nonlinearity for a given mode, with the α terms describing self-phase modulation (SPM) and cross-phase modulation (XPM) effects and the β terms characterizing the energy transfer between the modes. (Technically speaking, this qualitative distinction between α and β is only true in the limit of small losses [23]).

A. Losses

Equations (1) and (4) can be solved to study the steady-state conversion efficiency of the system [$\eta = |s_{p-}|^2/(|s_{0+}|^2 + |s_{m+}|^2)$] in response to incident light at the resonant cavity frequencies ($\omega_k = \omega_{ck}$), as was done in Ref. [41] in the ideal case of perfect frequency matching ($\omega_{cp} = 2\omega_{c0} - \omega_{cm}$), no losses ($\tau_k \neq \tau_{sk}$), and no SPM or CPM ($\alpha = 0$). In this ideal case, one can obtain analytical expressions for the maximum efficiency η^{max} and critical powers $P_0^{\text{crit}} = |s_{0+}^{\text{crit}}|^2$ and $P_m^{\text{crit}} = |s_{m+}^{\text{crit}}|^2$, at which 100% depletion of the total input power is attained [41]. Performing a similar calculation, but this time including the possibility of losses, we find

$$P_0^{\text{crit}} = \frac{4}{\tau_{s0}|\beta_0|\sqrt{\tau_m\tau_p\omega_m\omega_p}}, \quad (10)$$

$$\eta^{\text{max}} = \frac{\tau_p}{\tau_{sp}}\left(2 - \frac{\tau_{s0}}{\tau_0}\right)\frac{\omega_p}{2\omega_0}. \quad (11)$$

With respect to the lossless case, the presence of losses merely decreases the maximum achievable efficiency by a factor of $\tau_p/\tau_{sp}(2 - \tau_{s0}/\tau_0)$ while increasing the critical power P_0^{crit} by a factor of $\sqrt{\tau_{sm}\tau_{sp}/\tau_m\tau_p}$. As in the case of no losses, 100% depletion is only possible in the limit as $P_m \to 0$, from which it follows that the maximum efficiency is independent of τ_m. As noted in Ref. [41], the existence of a limiting efficiency (11) can also be predicted from the Manley-Rowe relations governing energy transfer in nonlinear systems [68] as can the limiting condition $P_m \to 0$. While theoretically this suggests that one should always employ as small a P_m as possible, as we show below, practical considerations make it desirable to work at a small but finite (nonnegligible) P_m.

B. Self-phase and cross-phase modulation

Unlike losses, the presence of SPM and XPM dramatically alters the frequency-conversion process. Specifically, a finite

α leads to a power-dependent shift in the effective cavity frequencies $\omega_{ck}^{\text{NL}} = \omega_{ck}(1 - \sum_j \alpha_{kj}|A_j|^2)$ that spoils both the frequency-matching condition as well as the coupling of the incident light to the corresponding cavity modes. One approach to overcome this difficulty is to choose or design the linear cavity frequencies to have frequency ω_{ck} slightly detuned from the incident frequencies ω_k, such that at the critical powers the effective cavity frequencies align with the incident frequencies and satisfy the frequency-matching condition [41]. Specifically, assuming incident light at ω_0 and ω_m, it follows by inspection of Eqs. (1) to (4) that preshifting the linear cavity resonances away from the incident frequencies according to the transformation

$$\omega_{c0}^{\text{crit}} = \frac{\omega_0}{1 - \alpha_{00}|a_0^{\text{crit}}|^2 - \alpha_{0m}|a_m^{\text{crit}}|^2 - \alpha_{0p}|a_p^{\text{crit}}|^2}, \quad (12)$$

$$\omega_{cm}^{\text{crit}} = \frac{\omega_m}{1 - \alpha_{m0}|a_0^{\text{crit}}|^2 - \alpha_{mm}|a_m^{\text{crit}}|^2 - \alpha_{mp}|a_p^{\text{crit}}|^2}, \quad (13)$$

$$\omega_{cp}^{\text{crit}} = \frac{2\omega_0 - \omega_m}{1 - \alpha_{p0}|a_0^{\text{crit}}|^2 - \alpha_{pm}|a_m^{\text{crit}}|^2 - \alpha_{pp}|a_p^{\text{crit}}|^2}, \quad (14)$$

yields the same steady-state critical solution obtained for $\alpha = 0$, where a_k^{crit} denotes the critical, steady-state cavity fields.

An alternative approach to excite the critical solution above in the presence of SPM and XPM is to detune the incident frequencies away from ω_{c0} and ω_{cm}, keeping the two cavity frequencies unchanged, while preshifting ω_{cp} to enforce frequency matching. Specifically, by inspection of Eqs. (12) to (14), it follows that choosing input-light frequencies

$$\omega_0^{\text{crit}} = \omega_{c0}\left(1 - \alpha_{00}|a_0^{\text{crit}}|^2 - \alpha_{0m}|a_m^{\text{crit}}|^2 - \alpha_{0p}|a_p^{\text{crit}}|^2\right), \quad (15)$$

$$\omega_m^{\text{crit}} = \omega_{cm}\left(1 - \alpha_{m0}|a_0^{\text{crit}}|^2 - \alpha_{mm}|a_m^{\text{crit}}|^2 - \alpha_{mp}|a_p^{\text{crit}}|^2\right), \quad (16)$$

and tuning ω_{cp} such that

$$\omega_{cp}^{\text{crit}} = \frac{2\omega_{c0}\left(1 - \sum \alpha_{0k}|a_k^{\text{crit}}|^2\right) - \omega_{cm}\left(1 - \sum \alpha_{mk}|a_k^{\text{crit}}|^2\right)}{1 - \sum \alpha_{pk}|a_k^{\text{crit}}|^2}, \quad (17)$$

yields the same steady-state critical solution above. This approach is advantageous in that the requirement that all three cavity frequencies be simultaneously and independently tuned (postfabrication) is removed in favor of tuning a single cavity mode. Given a scheme to tune the frequencies of the cavity modes that achieves perfect frequency matching at the critical power, what remains is to analyze the stability and excitability of the new critical solution, which can be performed using a straightforward linear stability analysis of the coupled-mode equations [38]. Before addressing these questions, however, it is important to address a more serious concern.

C. Frequency mismatch

Regardless of the tuning mechanism, in practice one can never fully satisfy perfect frequency matching (even when SPM and XPM can be neglected) due to fabrication imperfections. In general, one would expect the finite bandwidth to

mean that there is some tolerance $\sim 1/Q_p$ on any frequency mismatch $\Delta\omega = 2\omega_{c0} - \omega_{cm} - \omega_{cp} \lesssim \omega_{cp}/Q_{cp}$ [60]. However, here we find that instabilities and strong modifications of the cavity lineshapes arising from the particular nature of this nonlinear process lead to extreme, subbandwidth sensitivity to frequency deviations that must be carefully examined if one is to achieve high-efficiency operation.

To illustrate the effects of frequency mismatch, we first consider an ideal, lossless system with zero SPM and XPM ($\alpha = 0$) and with incident light at frequencies $\omega_0 = \omega_{c0}$ and $\omega_m = \omega_{cm}$, and powers P_0^{crit} and P_m, respectively. With the exception of α, the coupling coefficients and cavity parameters correspond to those of the 2D design described in Sec. III A. Figure 3 (top) shows the steady-state conversion efficiency η (solid lines) as a function of the frequency mismatch $\Delta_{cp} = \omega_{cp} - \omega_{cp}^{\text{crit}}$ away from perfect frequency matching, for multiple values of $P_m = \{0.001, 0.01, 0.1\}P_0^{\text{crit}}$, with dark gray (blue) and light gray (red) solid lines denoting stable and unstable steady-state fixed points. As shown, solutions come in pairs of stable and unstable fixed points, with the stable solution approaching the maximum efficiency η^{max} critical solution as $P_m \to 0$. Moreover, one observes that as Δ_{cp} increases for finite P_m, the stable and unstable fixed points approach and annihilate one other, with limit cycles appearing in their stead (an example of what is known as a "saddle-node homoclinic bifurcation" [69]). We stress that these bifurcations differ from the conventional Hopf bifurcations observed in optical parametric oscillators [70,71]. In a Hopf bifurcation, limit cycles are born when a fixed point becomes unstable, and are therefore associated with the presence of one or more unstable fixed points. In contrast, the limit cycles obtained here are not associated with any particular fixed points, but arise because two fixed points, one stable and the other unstable, annihilate each other at the onset of the bifurcation, a so-called saddle-node bifurcation. The limit cycle is therefore the remnant of the homoclinic orbit that connected the two fixed points, a so-called "saddle node-homoclinic bifurcation." The frequency mismatch at which this bifurcation occurs is proportional to P_m, so that, as $P_m \to 0$, the regime over which there exist high-efficiency steady states reduces to a single *fixed point* occurring at $\Delta_{cp} = 0$. Beyond this bifurcation point, the system enters a limit-cycle regime (shaded regions) characterized by periodic modulations of the output signal in time [37,38,72]. Interestingly, we find that the average efficiency of the limit cycles (dashed lines)

$$\bar{\eta} = \lim_{T \to \infty} \frac{1}{T} \int_0^T dt \, \eta(t), \qquad (18)$$

remains large $\sim \eta^{\text{max}}$ even when Δ_{cp} is several fractional bandwidths. The inset of Fig. 3 (top) shows the efficiency of this system as a function of time (in units of the lifetime τ_0) for large mismatch $\Delta_{cp} = 3\omega_{cp}^{\text{crit}}/2Q_p$. As expected, the modulation amplitude and period of the limit cycles depend on the input power and mismatch, and in particular we find that the amplitude goes to zero and the period diverges $\sim 1/\Delta_{cp}$ as $\Delta_{cp} \to 0$. This behavior is observed across a wide range of P_m, with larger P_m leading to lower $\bar{\eta}$ and larger amplitudes. For small-enough mismatch, the modulation frequency enters the THz regime, in which case standard
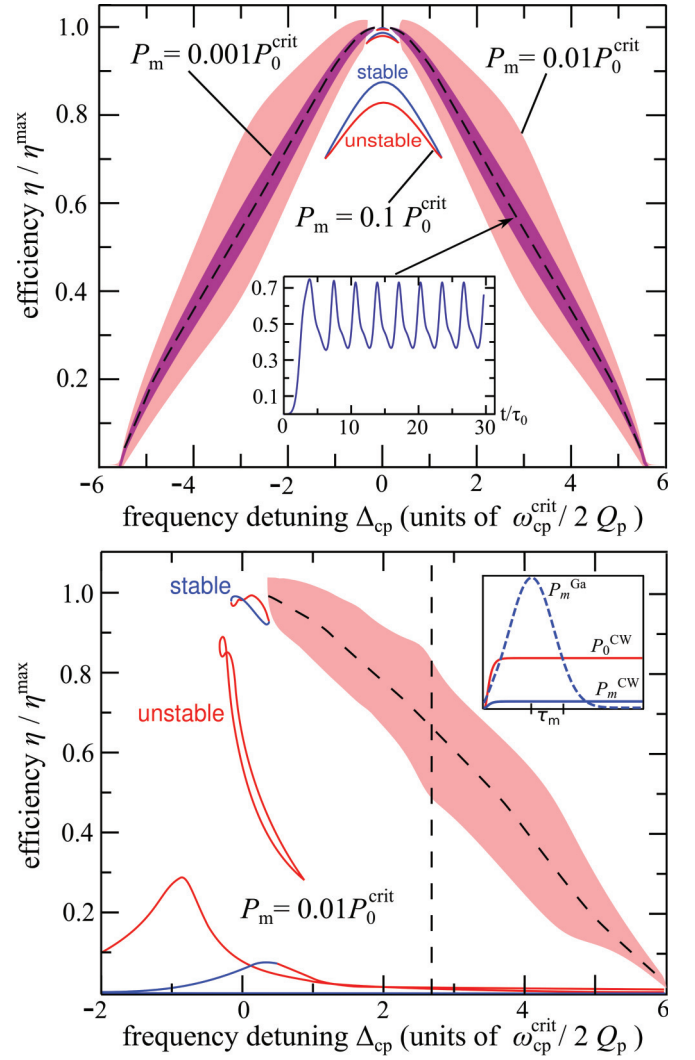

FIG. 3. (Color online) (Top) Steady-state conversion efficiency η (normalized by the maximum achievable efficiency η^{max}) as a function of frequency mismatch $\Delta_{cp} = \omega_{cp} - \omega_{cp}^{\text{crit}}$ (in units of $\omega_{cp}^{\text{crit}}/2Q_p$), for the cavity system depicted in Fig. 5, but in the absence of SPM and XPM ($\alpha = 0$). Incident frequencies are chosen to be $\omega_0 = \omega_0^{\text{crit}}$ and $\omega_m = \omega_m^{\text{crit}}$, with corresponding powers $P_0 = P_0^{\text{crit}}$ and P_m, where we consider multiple $P_m = \{0.1, 0.01, 0.001\}P_0^{\text{crit}}$. Note that since $\alpha = 0$, critical frequencies are independent of incident powers, so that $\omega_0^{\text{crit}} = \omega_{c0}$, $\omega_m^{\text{crit}} = \omega_{cm}$, and $\omega_{cp}^{\text{crit}} = 2\omega_{c0} - \omega_{cm}$. Dark gray (blue) and light gray (red) solid lines denote stable and unstable fixed points, whereas shaded areas indicate regimes lacking fixed point solutions and exhibiting limit-cycle behavior, shown only for $P_m = \{0.01, 0.001\}P_0^{\text{crit}}$, with smaller amplitudes corresponding to smaller P_m. Dashed lines denote the average efficiency of the limit cycles $\bar{\eta}$, whereas the top and bottom of the shaded regions denote the maximum and minimum efficiency per period. The inset shows the efficiency as a function of time for a typical limit cycle, obtained at $\Delta_{cp} \approx 3\omega_{cp}^{\text{crit}}/2Q_p$. (Bottom) η and $\bar{\eta}$ for the same system above, but in the presence of SPM and XPM ($\alpha \neq 0$), and only for $P_m = 0.01P_0^{\text{crit}}$. Note that additional stable and unstable fixed points arise due to the nonzero α, and that limit-cycle behaviors arise only for $\Delta_{cp} > 0$. Inset shows the temporal shape of the incident power needed to excite the desired limit cycles, corresponding to a Gaussian pulse superimposed over continuous wave inputs.

rectifications procedures [73] can be applied to extract the useful THz oscillations [4,5,74–77].

Frequency mismatch leads to similar effects for finite α, including homoclinic bifurcations and corresponding high-efficiency limit cycles that persist even for exceedingly large frequency mismatch. One important difference, however, is that the redshift associated with SPM and XPM creates a strongly asymmetrical lineshape that prevents high-efficiency operation for $\Delta_{cp} < 0$. Figure 3 (bottom) shows the stable and unstable fixed points (solid lines) and limit cycles (dashed regions) as a function of Δ_{cp} for the same system of Fig. 3 (top) but with finite α and for two values of $P_m = \{0.001, 0.01\} P_0^{\text{crit}}$. As before, the coupling coefficients and cavity parameters correspond to those of the 2D design described in Sec. III A. Here, in contrast to the $\alpha = 0$ case, the critical incident frequencies ω_0^{crit} and ω_m^{crit} are chosen according to Eqs. (15) and (16) to counter the effects of SPM and XPM, and are therefore generally different from ω_{c0} and ω_{cm}. Aside from the asymmetrical lineshape, one important difference from the $\alpha = 0$ case is the presence of additional stable and unstable low-efficiency solutions. Multistability complicates matters since, depending on the initial conditions, the system can fall into different stable solutions and in particular, simply turning on the source at the critical input power may result in an undesirable low-efficiency solution. One well-known technique that allows such a system to lock into the desired high-efficiency solutions is to superimpose a gradual exponential turn-on of the pump with a Gaussian pulse of larger amplitude [37]. We found that a single Gaussian pulse with a peak power of $4P_0^{\text{crit}}$ and a temporal width $\sim\tau_m$, depicted in the right inset of Fig. 3 (bottom), is sufficient to excite high-efficiency limit cycles in the regime $\Delta_{cp} > 0$.

Despite their high efficiencies (even for large $\Delta_{cp} \gtrsim 1$), the limit-cycle solutions above leave something to be desired. Depending on the application, it may be desirable to operate at high-efficiency fixed points. One way to achieve this for nonzero frequency mismatch is to abandon the critical solution and instead choose incidence parameters that exploit SPM and XPM to enforce perfect frequency matching and 100% depletion of the pump, i.e.,

$$\omega_{cp}^{\text{NL}} + \omega_{cm}^{\text{NL}} = 2\omega_{c0}^{\text{NL}}, \tag{19}$$

$$s_{0-} = 0. \tag{20}$$

Specifically, enforcing Eqs. (19) and (20) by solving Eqs. (1) to (4) for $\omega_0^{\text{dep}}, \omega_m^{\text{dep}}, P_0^{\text{dep}}$, and P_m^{dep}, we obtain a *depleted* steady-state solution a_k^{dep} that, in contrast to the critical solution a_k^{crit}, yields a steady-state efficiency that corresponds to 100% depletion of the pump regardless of frequency mismatch. Note that we are not explicitly maximizing the conversion efficiency, but rather enforcing complete conversion of pump energy in the presence of frequency mismatch, at the expense of a nonnegligible input P_m^{dep}. Figure 4 shows the depleted steady-state efficiency η^{dep} (solid line) and corresponding incident powers (solid circles and dashed line) as a function of Δ_{cp}, for the same system of Fig. 3 (bottom). We find that for most parameters of interest, depleted efficiencies and powers are uniquely determined by Eqs. (19) and (20). As expected, the optimal efficiency occurs at $\Delta_{cp} = 0$ and corresponds to
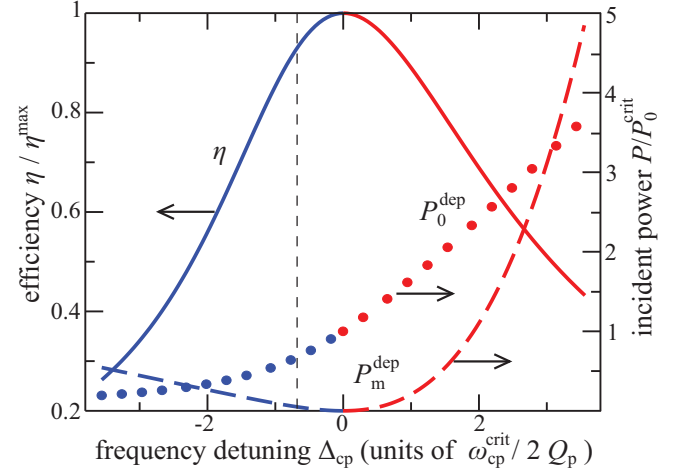

FIG. 4. (Color online) Steady-state conversion efficiency (normalized by the maximum achievable efficiency η^{max}) and required incident powers P_0^p and P_m^m (normalized by the critical power P_0^{crit}) corresponding to depleted steady states of the system of Fig. 5, as a function of frequency mismatch $\Delta_{cp} = \omega_{cp} - \omega_{cp}^{\text{crit}}$ (in units of $\omega_{cp}^{\text{crit}}/2Q_p$). As described in Sec. III A 2, depleted states yield 100% depletion of P_0, and are excited by appropriate combinations of incident frequencies $\omega_k = \omega_k^{\text{dep}}$ and powers $P_k = P_k^{\text{dep}}$. Dark gray (blue) and light gray (red) lines denote stable and unstable solutions, with solid lines, dashed lines, and circles, denoting η, P_m^{dep}, and P_0^{dep}, respectively.

the critical solution, so that $P_0^{\text{dep}} = P_0^{\text{crit}}$, $P_m^{\text{dep}} = P_m^{\text{crit}} = 0$, and $\eta^{\text{dep}} = \eta^{\text{max}}$. For finite $\Delta_{cp} \neq 0$, the optimal efficiencies are lower due to the finite P_m^{dep}, but there exists a broad range of Δ_{cp} over which one obtains relatively high efficiencies $\sim\eta^{\text{max}}$. Power requirements P_0^{dep} and P_m^{dep} follow different trends depending on the sign of Δ_{cp}. Away from zero detuning, P_m^{dep} can only increase, whereas P_0^{dep} decreases for $\Delta_{cp} < 0$ and increases for $\Delta_{cp} > 0$. In the latter case, the total input power exceeds P_0^{crit} leading to the observed instability of the fixed-point solutions.

Finally, we point out that limit cycles and depleted steady states reside in roughly complementary regimes. Although no stable high-efficiency fixed points can be found in the $\Delta_{cp} > 0$ regime, it is nevertheless possible to excite high-efficiency limit cycles. Conversely, although no such limit cycles exist for $\Delta_{cp} < 0$, it is possible in that case to excite high-efficiency depleted steady states.

III. FDTD SIMULATIONS AND NANOBEAM DESIGNS

In this section, we consider concrete and realistic cavity designs in two and three dimensions, and validate the predictions of our TCMT by performing exact nonlinear FDTD simulations in two dimensions. We show that by choosing slightly different designs, one can explore high-efficiency conversion in either the limit-cycle or depleted steady-state regimes. Our designs are based on a particular class of PhC nanobeam structures, depicted schematically in Figs. 5 and 2, where a cavity is formed by the introduction of a defect in a lattice of air holes in dielectric, and coupled to
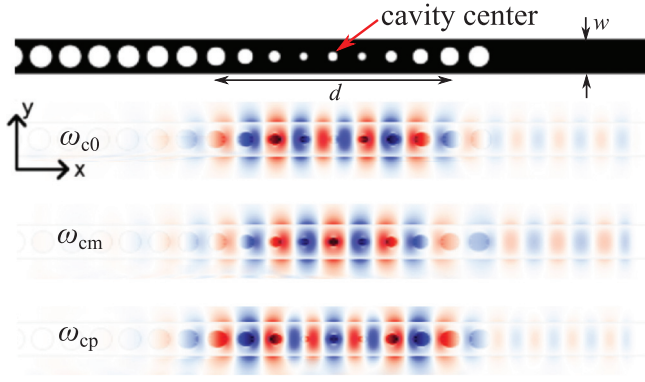
FIG. 5. (Color online) Schematic of 2D triply resonant cavity design involving a PhC nanobeam of refractive index $n = 3.4$, width $w = 1.2a$, and adiabatically varying hole radii (see text). The effective cavity length $d = 6.6a$ and the radius of the central hole R_0 are chosen so as to fine-tune the relative frequency spacing and lifetimes of the modes. Also shown are the E_y electric field components of the three modes relevant to DFWM. The cavity is coupled to a waveguide formed by the removal of holes to the right of the defect.

an adjacent waveguide formed by the removal of holes on one side of the defect. We restrict our analysis to dielectric materials with high nonlinearities at near-infrared and mid-infrared wavelengths [1], and in particular focus on undoped silicon, whose refractive index $n \approx 3.4$ and Kerr susceptibility $\chi^{(3)} \sim 10^{-18}$ m^2/V^2 [78].

Before delving into the details of any particular design, we first describe the basic considerations required to achieve the desired high-efficiency characteristics. To begin with, we seek modes that approximately satisfy $\omega_{cm} + \omega_{cp} = 2\omega_{c0}$. The final cavity design, incorporating SPM and XPM, is then obtained by additional tuning of the mode frequencies as described by the predictions of the coupled-mode theory (CMT). Second, we seek modes that have large nonlinear overlap β, determined by Eq. (8). (Ideally, one would also optimize the cavity

design to reduce α/β, but such an approach falls beyond the scope of this work.) Note that the overlap integral β replaces the standard "quasiphase matching" requirement in favor of constraints imposed by the symmetries of the cavity [1]. In our case, the presence of reflection symmetries means that the modes can be classified as either even or odd and also as "transverse electric (TE)-like" ($\mathbf{E} \cdot \hat{\mathbf{z}} \approx 0$) or "transverse magnetic (TM)-like" ($\mathbf{H} \cdot \hat{\mathbf{z}} \approx 0$) [79], and hence only certain combinations of modes will yield nonzero overlap. It follows from Eq. (8) that any combination of even or odd modes will yield nonzero overlap so long as $\mathbf{E}_m$ and $\mathbf{E}_p$ have the same parity, and as long as all three modes have similar polarizations: modes with different polarization will cause the term $\sim (\mathbf{E}_0^* \cdot \mathbf{E}_m)(\mathbf{E}_0^* \cdot \mathbf{E}_p)$ in Eq. (8) to vanish. Third, to minimize radiation losses, we seek modes whose radiation lifetimes are much greater than their total lifetimes, as determined by any desired operational bandwidth. In what follows, we assume operational bandwidths with $Q \sim 10^3$. Finally, we require that our system supports a single input or output port for light to couple in or out of the cavity, with coupling lifetimes $Q_{sk} \ll Q_{rk}$ to have negligible radiation losses.

A. 2D design

To explore both high-efficiency limit-cycle and steady-state behaviors, we consider two separate 2D cavity designs, each resulting in different frequency mismatch but similar lifetimes and coupling coefficients. (Note that by "2D" we mean that electromagnetic fields are taken to be uniform in the z direction.) The two cavities follow the same backbone design shown in Fig. 5 which supports three TE-polarized modes ($\mathbf{H} \cdot \hat{\mathbf{z}} = 0$) with radiative lifetimes $Q_0^{\text{rad}} = 6 \times 10^4, Q_m^{\text{rad}} = 6 \times 10^4$, and $Q_p^{\text{rad}} = 3 \times 10^3$, and total lifetimes $Q_0 = 1200, Q_m = 1100$, and $Q_p = 700$, respectively. The nonlinear coupling coefficients are calculated from the linear modal profiles (shown on the inset of Fig. 5) via Eqs. (8) and (7), and are given by

$$\beta = (23.69 + 5.84i) \times 10^{-5} \left(\frac{\chi^{(3)}}{\epsilon_0 a^2 h} \right),$$

$$\alpha_{00} = 4.935 \times 10^{-4} \left(\frac{\chi^{(3)}}{\epsilon_0 a^2 h} \right), \quad \alpha_{mm} = 5.096 \times 10^{-4} \left(\frac{\chi^{(3)}}{\epsilon_0 a^2 h} \right),$$

$$\alpha_{pp} = 4.593 \times 10^{-4} \left(\frac{\chi^{(3)}}{\epsilon_0 a^2 h} \right), \quad \alpha_{0m} = 6.540 \times 10^{-4} \left(\frac{\chi^{(3)}}{\epsilon_0 a^2 h} \right),$$

$$\alpha_{0p} = 5.704 \times 10^{-4} \left(\frac{\chi^{(3)}}{\epsilon_0 a^2 h} \right), \quad \alpha_{mp} = 5.616 \times 10^{-4} \left(\frac{\chi^{(3)}}{\epsilon_0 a^2 h} \right),$$

where the additional factor of h allows comparison to the realistic 3D structure below and accounts for finite nanobeam thickness (again, assuming uniform fields in the z direction). Compared to the optimal $\beta^{\text{max}} = \frac{3}{4n^4 wd} \left(\frac{\chi^{(3)}}{\epsilon_0 h} \right)$, corresponding to modes with uniform fields inside and zero fields outside the cavity, we find that $\beta = 5.5 \times 10^{-3} \beta^{\text{max}}$ is significantly smaller due to the fact that these TE modes are largely concentrated

in air. In the 3D design section below, we choose modes with peaks in the dielectric regions, which leads to much larger $\beta \approx 0.4 \beta^{\text{max}}$.

To arrive at this 2D design, we explored a wide range of defect parameters, with the defect formed by modifying the radii of a finite set of holes in an otherwise periodic lattice of air holes of period a and radius $R = 0.36a$ in a

dielectric nanobeam of width $w = 1.2a$ and index of refraction $n = 3.4$. The defect was parametrized via an exponential adiabatic taper of the air-hole radii r, in accordance with the formula $r(x) = R(1 - \frac{3}{4}e^{-\frac{4|x|^2}{d^2}})$, where the parameter d is an "effective cavity length." Such an adiabatic taper is chosen to reduce radiation and scattering losses at the interfaces of the cavity [80]. Removing holes on one side of the defect couples light to a waveguide with decay rate $\sim 1/Q_s$ determined by the number of holes removed [81–83].

1. Limit cycles

In this section, we consider a design supporting high-efficiency limit cycles. Choosing $R_0 = 0.149a$, we obtain critical parameters $\omega_0^{\mathrm{crit}} = 0.2319(\frac{2\pi c}{a})$, $\omega_m^{\mathrm{crit}} = 0.2121(\frac{2\pi c}{a})$, $\omega_{cp}^{\mathrm{crit}} = 0.2530(\frac{2\pi c}{a})$, and $P_0^{\mathrm{crit}} = 10^{-3}(\frac{2\pi c\epsilon_0 ah}{\chi^{(3)}})$, corresponding to frequency mismatch $\Delta_{cp} \approx 3\omega_{cp}^{\mathrm{crit}}/2Q_p$ and critical efficiency $\eta^{\mathrm{max}} = 0.51$. Choosing a small but finite $P_m = 0.01P_0^{\mathrm{crit}}$, it follows from Fig. 3 (dashed line) that the system will support limit cycles with average efficiencies $\bar{\eta} \approx 0.65\eta^{\mathrm{max}}$. To excite these solutions, we employed the priming technique described in Sec. II C. Figure 6 shows $\bar{\eta}$ as a function of P_0, for incident frequencies $\omega_k = \omega_k^{\mathrm{crit}}$ determined by Eqs. (15) and (16), as computed by our TCMT (dotted gray line) as well as by fully vectorial nonlinear FDTD simulations (solid circles). The two show excellent agreement. For $0.7 < P_0/P_0^{\mathrm{crit}} < 3$, we observe limit cycles with relatively high $\bar{\eta}$, in accordance with the TCMT predictions, whereas outside of this regime, we find that the system invariably falls
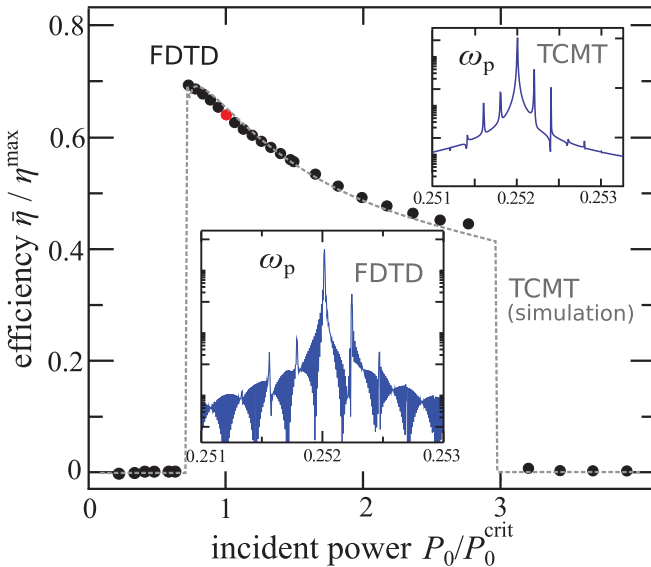
into low-efficiency fixed points. The periodic modulation of the limit cycles means that instead of a single peak, the spectrum of the output signal consists of equally spaced Fourier peaks that decrease in magnitude away from ω_p. The top and bottom insets of Fig. 6 show the corresponding frequency spectra of the TCMT and FDTD output signals around ω_p, for a particular choice of $P_0 \approx P_0^{\mathrm{crit}}$ [light gray (red) circle], showing agreement both in the relative magnitude and spacing $\approx 2.5 \times 10^{-3}(\frac{2\pi c}{a})$ of the peaks.

2. Depleted steady states

In this section, we consider a design supporting high-efficiency, depleted steady states. Choosing $R_0 = 0.143a$, one obtains critical parameters $\omega_0^{\mathrm{crit}} = 0.2320(\frac{2\pi c}{a})$, $\omega_m^{\mathrm{crit}} = 0.2118(\frac{2\pi c}{a})$, $\omega_{cp}^{\mathrm{crit}} = 0.2532(\frac{2\pi c}{a})$, and $P_0^{\mathrm{crit}} = 10^{-3}(\frac{2\pi c\epsilon_0 ah}{\chi^{(3)}})$, corresponding to frequency mismatch $\Delta_{cp} \approx -0.6\omega_{cp}^{\mathrm{crit}}/2Q_p$ and critical efficiency $\eta^{\mathrm{max}} = 0.51$. Choosing incident frequencies $\omega_0^{\mathrm{dep}} = 0.2320(\frac{2\pi c}{a})$, $\omega_m^{\mathrm{dep}} = 0.2119(\frac{2\pi c}{a})$, and incident powers $P_0^{\mathrm{dep}} \approx 0.7P_0^{\mathrm{crit}}$ and $P_m^{\mathrm{dep}} \approx 0.04P_0^{\mathrm{crit}}$, it follows from Fig. 4 (dashed line) that the system supports stable, depleted steady states with efficiencies $\approx 0.95\eta^{\mathrm{max}}$. Figure 7
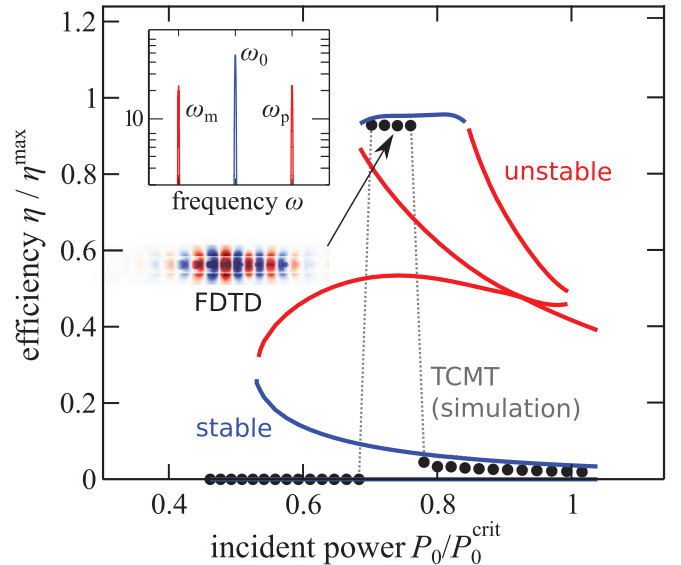

FIG. 7. (Color online) Conversion efficiency η (normalized by the maximum achievable efficiency η^{max}) of depleted states as a function of power P_0 (normalized by P_0^{crit}), at incident frequencies ω_0^{dep} and ω_m^{dep}, and a fixed power $P_m^{\mathrm{dep}} \approx 0.2P_0^{\mathrm{crit}}$. The modal parameters are obtained from the 2D cavity of Fig. 5, with $R_0 = 0.143a$ leading to a detuning $\Delta_{cp} \approx -0.6\omega_{cp}^{\mathrm{crit}}/2Q_p$ corresponding to the dashed line in Fig. 4. E_y component of the steady-state electric field inside the cavity is shown as an inset (left, bottom). Solid circles and dotted gray lines denote FDTD and TCMT, while dark gray (blue) and light gray (red) lines denote stable and unstable steady states. Inset (left, top) shows the spectral profile (in arbitrary units) of the system, showing full depletion of the pump [dark gray (blue)] and correspondingly high conversion of the signal and idler frequencies [light gray (red)]. For $P_0 \gtrsim 0.8P_0^{\mathrm{crit}}$, the system becomes ultrasensitive to the priming parameters, in which case high-efficiency solutions can only be excited by adiabatic tuning of the pump power (see text).

FIG. 6. (Color online) Average conversion efficiency $\bar{\eta}$ (normalized by the maximum achievable efficiency η^{max}) of limit cycles as a function of power P_0 (normalized by P_0^{crit}) at the critical frequencies ω_0^{crit} and ω_m^{crit} and a fixed $P_m = 0.01P_0^{\mathrm{crit}}$. The modal parameters are obtained from the 2D cavity of Fig. 5, with chosen $R_0 = 0.149a$ leading to a detuning $\Delta_{cp} \approx 3\omega_{cp}^{\mathrm{crit}}/2Q_p$ corresponding to the dashed line in Fig. 3 (bottom). Solid circles and dotted gray lines denote results as computed by FDTD and TCMT. Insets show the spectra of the output light for a given P_0 [light gray (red) circle], and for both FDTD and TCMT.

shows the efficiency of the system as a function P_0, with all other incident parameters fixed to the depleted-solution values above, where dark gray (blue) and light gray (red) lines denote stable and unstable solutions, respectively. As before, we employ the priming technique of Sec. II C to excite the desired high-efficiency solutions and obtain excellent agreement between the TCMT (dotted gray line) and FDTD simulations (solid circles). Exciting the high-efficiency solutions by steady-state input "primed" with a Gaussian pulse is convenient in FDTD because it leads to relatively short simulations, but is problematic for $P_0 > 0.8 P_0^{\text{crit}}$, where the system becomes very sensitive to the priming parameters and it becomes impractical to find the optimal source conditions in Fig. 7. Alternatively, one could also employ other, more robust techniques to excite the high-efficiency solution, such as by adiabatically tuning the pump power [37].

B. 3D design

In addition to paving the way for a promising nanobeam cavity design, the 2D nonlinear FDTD simulations of the previous section demonstrate the validity and predictions of the TCMT and the proposed approaches for overcoming frequency mismatch. In this section, we consider a full 3D design, depicted in Fig. 2, as a feasible candidate for experimental realization. The cavity supports three TE$_{00}$ modes ($\mathbf{E}_z = 0$ at $z = 0$) of frequencies $\omega_{c0} = 0.2848(\frac{2\pi c}{a})$, $\omega_{cm} = 0.2801(\frac{2\pi c}{a})$ and $\omega_{cp} = 0.2895(\frac{2\pi c}{a})$, radiative lifetimes $Q_0^{\text{rad}} = 10^6$, $Q_m^{\text{rad}} = 3 \times 10^4$, $Q_p^{\text{rad}} = 2 \times 10^4$. As before, the total lifetimes can be adjusted by removing air holes to the right or left of the defect, which would allow coupling to the resulting in-plane waveguides. (Alternatively, one might consider an out-of-plane coupling mechanism in which a fiber carrying incident light at both ω_0 and/or ω_m is brought in close proximity to the cavity [81,84].) In what follows, we do not consider any one particular coupling channel and focus instead on the isolated cavity design. Nonlinear coupling coefficients are calculated from the linear modal profiles (shown on the inset of Fig. 2) via Eqs. (9) and (7), and are given by

$$\beta = 2 \times 10^{-4} \left(\frac{\chi^{(3)}}{\epsilon_0 a^3} \right),$$

$$\alpha_{00} = 8.1 \times 10^{-4} \left(\frac{\chi^{(3)}}{\epsilon_0 a^3} \right), \quad \alpha_{mm} = 4.6 \times 10^{-4} \left(\frac{\chi^{(3)}}{\epsilon_0 a^3} \right),$$

$$\alpha_{pp} = 11.5 \times 10^{-4} \left(\frac{\chi^{(3)}}{\epsilon_0 a^3} \right), \quad \alpha_{0m} = 6.2 \times 10^{-4} \left(\frac{\chi^{(3)}}{\epsilon_0 a^3} \right),$$

$$\alpha_{0p} = 12.7 \times 10^{-4} \left(\frac{\chi^{(3)}}{\epsilon_0 a^3} \right), \quad \alpha_{mp} = 5.5 \times 10^{-4} \left(\frac{\chi^{(3)}}{\epsilon_0 a^3} \right).$$

Note that here, and in contrast to the 2D design of Sec. III A, we chose modes whose amplitudes are concentrated in the dielectric regions, leading to appreciably larger $\beta \approx 0.4 \beta^{\text{max}}$.

To arrive at the above 3D design, we explored a cavity parametrization similar to the one described by the authors of Ref. [85]. Specifically, we employed a suspended nanobeam of width $w = a$, thickness $h = 0.51a$, and refractive index $n = 3.4$. The beam is schematically divided into a set of $2N$ lattice segments, each having length a_i, $i \in \{\pm 1, \ldots, \pm N\}$ and

corresponding air-hole radii $R_i = 0.3 a_i$, where a_1 (a_{-1}) is the length of the lattice segment immediately to the right (left) of the beam's center. The cavity defect is induced via a linear taper of a_i over a chosen set of $2\bar{N}$ segments, according to the formula

$$a_i = a \left(f_a + \frac{(1 - f_a)}{(\bar{N} - 1)} (|i| - 1) \right), \quad |i| \leqslant \bar{N}$$

$$= a, \qquad\qquad\qquad\qquad |i| > \bar{N}.$$

To arrive at our particular design, we chose $f_a = 0.85$, $N = 21$, $\bar{N} = 9$ and varied the central cavity length L to obtain the desired TE$_{00}$ modes. Assuming total modal lifetimes $Q_0 = 8500$, $Q_m = 3000$, and $Q_p = 3000$ and using these design parameters, we obtain critical parameters $\omega_0^{\text{crit}} = 0.2843(\frac{2\pi c}{a})$, $\omega_m^{\text{crit}} = 0.2798(\frac{2\pi c}{a})$, $\omega_{cp}^{\text{crit}} = 0.2895(\frac{2\pi c}{a})$, and $P_0^{\text{crit}} = 5 \times 10^{-5} (\frac{2\pi c \epsilon_0 a^2}{\chi^{(3)}})$, corresponding to frequency mismatch $\Delta_{cp} \approx -0.07 \omega_{cp}^{\text{crit}}/(2 Q_p)$ and $\eta^{\text{max}} = 0.42$. Note that because the radiative losses in this system are nonnegligible, the maximum efficiency of this system is $\approx 82\%$ of the optimal achievable efficiency $= \omega_p/(2\omega_0) \approx 0.51$. At these small Δ_{cp}, we find that depletion of the pump is readily achieved through the critical parameters associated with perfect frequency matching. However, as illustrated in Sec. III A 1, one can also choose a design that supports high-efficiency limit cycles.

1. Power requirements

Thus far, we have expressed the power requirements of this system in dimensionless units of $2\pi c \epsilon_0 a^2/\chi^{(3)}$. Choosing to operate at telecom wavelengths $\lambda_{c0} \equiv 2\pi c/\omega_{c0} = 1.5\,\mu\text{m}$, with corresponding $n \approx 3.4$ and $\chi^{(3)} = 2.8 \times 10^{-18}\,\text{m}^2/\text{V}^2$ [1], we find that $a = 0.2848 \times 1500 = 427$ nm and $P_0^{\text{crit}} \approx 50$ mW. We note, however, that although our analysis above incorporates effects arising from linear losses (e.g., due to material absorption or radiation), it neglects important and detrimental sources of nonlinear losses in the telecom range, including two-photon and free-carrier absorption [86,87]. Techniques that mitigate the latter exist, e.g., reverse biasing [88], but in their absence it may be safer to operate in the spectral region below the half-band-gap of Si [78]. One possibility is to operate at $\lambda_{c0} = 2.2\,\mu\text{m}$, where $\chi^{(3)} \approx 1.5 \times 10^{-18}\,\text{m}^2/\text{V}^2$ [78], leading to $a = 627$ nm, and approximately four-times larger $P_0^{\text{crit}} \approx 200$ mW. For a more detailed analysis of nonlinear absorption in triply resonant systems, the reader is referred to Ref. [89]. While that work does not consider the effects of nonlinear dispersion, SPM and XPM, or frequency mismatch, it does provide upper bounds on the maximum efficiency in the presence of two-photon and free-carrier absorption.

IV. CONCLUDING REMARKS

In conclusion, by combining TCMT with fully nonlinear FDTD simulations, we have demonstrated the possibility of achieving highly efficient DFWM at low input powers (~ 50 mW) and large bandwidths ($Q \sim 1000$) in a realistic and chip-scale (μm) nanophotonic platform (silicon nanobeam cavity). Our theoretical analysis extends the initial work of the authors of Ref. [41] by incorporating and analyzing important effects arising from linear losses, SPM and XPM,

as well as mismatch of the cavity-mode frequencies, e.g., such as those that arise from fabrication imperfections, where the latter was shown to lead to a variety of interesting dynamical behaviors, including limit cycles that arise in the presence of infinitesimally small frequency mismatch near critical solutions. Although power requirements in the tens of mWs are not often encountered in conventional chip-scale Si nanophotonics, they are comparable if not smaller than those employed in conventional centimeter-scale DFWM schemes [88,90,91]. Our proof-of-concept design demonstrates that full cavity-based DFWM not only reduces device dimensions down to μm scales, but also allows depletion of the pump with efficiencies close to unity. Compared to conventional integrated whispering-gallery-mode (WGM) resonators [22,92,93], nanobeam cavities offer much smaller mode volumes, $\sim(\frac{\lambda}{n})^3$ in nanobeams as compared to $\sim 100(\frac{\lambda}{n})^3$ in WGM cavities, and therefore allow exploration of these

processes at low powers and much larger bandwidths (which is especially important in this system due to its sensitivity to frequency mismatch). From a fabrication viewpoint, they are also desirable in that they allow for minimal footprint and maximal device density on chip. Finally, we emphasize that there is considerable room for additional design optimization. For instance, we find that increasing the radiative lifetimes of the signal and converted modes (currently almost two orders of magnitudes lower than the pump) can significantly lower the power requirements of the system.

[1] R. W. Boyd, *Nonlinear Optics* (Academic, San Diego, CA, 1992).

[2] J. Hald, Opt. Commun. **197**, 169 (2001).

[3] R. Lifshitz, A. Arie, and A. Bahabad, Phys. Rev. Lett. **95**, 133901 (2005).

[4] Y. A. Morozov, I. S. Nefedov, V. Y. Aleshkin, and I. V. Krasnikova, Semiconductors **39**, 113 (2005).

[5] K.-L. Yeh, M. C. Hoffmann, J. Hebling, and K. A. Nelson, Appl. Phys. Lett. **90**, 171121 (2007).

[6] J. Hebling, A. G. Stepanov, G. Almasi, B. Bartal, and J. Kuhl, Appl. Phys. B **78**, 593 (2004).

[7] Z. Ruan, G. Veronis, K. L. Vodopyanov, M. M. Fejer, and S. Fan, Opt. Express **17**, 13502 (2009).

[8] R. H. Stolen and J. E. Bjorkholm, IEEE J. Quantum Electron. **18**, 1062 (1982).

[9] N. M. Kroll, Phys. Rev. **127**, 1207 (1962).

[10] R. H. Stolen, E. P. Ippen, and A. R. Tynes, Appl. Phys. Lett. **20**, 62 (1972).

[11] S. A. Akhmanov, A. P. Sukhorukov, and R. V. Khokhlov, Soviet Phys. JETP **23**, 6 (1966).

[12] R. A. Fisher, *Optical Phase Conjugation* (Academic, New York, 1983).

[13] G. Contestabile, M. Presi, and E. Ciaramella, IEEE Photon. Tech. Lett. **16**, 7 (2004).

[14] S. J. B. Yoo, J. Lightwave Tech. **14**, 955 (1996).

[15] K. Gallo and G. Assanto, Appl. Phys. Lett. **79**, 314 (2001).

[16] H. Lira, Z. Yu, S. Fan, and M. Lipson, Phys. Rev. Lett. **109**, 033901 (2012).

[17] Y. Akahane, T. Asano, B.-S. Song, and S. Noda, Nature (London) **425**, 944 (2003).

[18] V. R. Almeida, C. A. Barrios, R. R. Panepucci, and M. Lipson, Nature (London) **431**, 1081 (2004).

[19] Y. A. Vlasov, M. O'Boyle, H. F. Hamann, and S. J. McNab, Nature (London) **438**, 65 (2005).

[20] B.-S. Song, S. Noda, T. Asano, and Y. Akahane, Nat. Mater. **4**, 207 (2005).

[21] P. B. Deotare, M. W. McCutcheon, I. W. Frank, M. Khan, and M. Loncar, Appl. Phys. Lett. **94**, 121106 (2009).

[22] T. J. Kippenberg, S. M. Spillane, and K. J. Vahala, Phys. Rev. Lett. **93**, 083904 (2004).

[23] A. Rodriguez, M. Soljačić, J. D. Joannopulos, and S. G. Johnson, Opt. Express **15**, 7303 (2007).

[24] M. Soljačić, M. Ibanescu, S. G. Johnson, Y. Fink, and J. D. Joannopoulos, Phys. Rev. E **66**, 055601(R) (2002).

[25] V. S. Ilchenko, A. A. Savchenkov, A. B. Matsko, and L. Maleki, Phys. Rev. Lett. **92**, 043903 (2004).

[26] J. U. Fürst, D. V. Strekalov, D. Elser, M. Lassen, U. L. Andersen, C. Marquardt, and G. Leuchs, Phys. Rev. Lett. **104**, 153901 (2010).

[27] X. Liu, R. M. Osgood, Y. A. Vlasov, and W. M. J. Green, Nat. Photon. **4**, 557 (2010).

[28] M. A. Foster, A. C. Turner, J. E. Sharping, B. S. Schmidt, M. Lipson, and A. L. Gaeta, Nature (London) **441**, 960 (2006).

[29] M. Bieler, IEEE J. Select. Top. Quant. Electron. **14**, 458 (2008).

[30] R. E. Hamam, M. Ibanescu, E. J. Reed, P. Bermel, S. G. Johnson, E. Ippen, J. D. Joannopoulos, and M. Soljacic, Opt. Express **12**, 2102 (2008).

[31] P. Bermel, A. Rodriguez, J. D. Joannopoulos, and M. Soljacic, Phys. Rev. Lett. **99**, 053601 (2007).

[32] J. Bravo-Abad, S. Fan, S. G. Johnson, J. D. Joannopoulos, and M. Soljacic, J. Lightwave Tech. **25**, 2539 (2007).

[33] L. Caspani, D. Duchesne, K. Dolgaleva, S. J. Wagner, M. Ferrera, L. Razzari, A. Pasquazi, M. Peccianti, D. J. Moss, J. S. Aitchison *et al.*, J. Opt. Soc. Am. B **28**, A67 (2011).

[34] F. S. Felber and J. H. Marburger, Appl. Phys. Lett. **28**, 731 (1976).

[35] Y. Dumeige and P. Feron, Phys. Rev. A **84**, 043847 (2011).

[36] R. G. Smith, IEEE J. Quantum Electron. **6**, 215 (1970).

[37] H. Hashemi, A. W. Rodriguez, J. D. Joannopoulos, M. Soljacic, and S. G. Johnson, Phys. Rev. A **79**, 013812 (2009).

[38] P. D. Drummond, K. J. McNeil, and D. F. Walls, Optica Acta. **27**, 321 (1980).

[39] K. Grygiel and P. Szlatchetka, Opt. Comm. **91**, 241 (1992).

[40] E. Abraham, W. J. Firth, and J. Carr, Phys. Lett. A **69**, 47 (1982).

[41] D. M. Ramirez, A. W. Rodriguez, H. Hashemi, J. D. Joannopoulos, M. Soljačić, and S. G. Johnson, Phys. Rev. A **83**, 033834 (2011).

[42] K. R. Parameswaran, J. R. Kurz, R. V. Roussev, and M. M. Fejer, Opt. Express **27**, 1 (2002).

[43] P. S. Kuo and G. S. Solomon, Opt. Express **19**, 16898 (2011).

[44] M. Ferrera, L. Razzari, D. Duchesne, R. Morandotti, Z. Yang, M. Liscidini, J. E. Sipe, S. Chu, B. E. Little, and D. J. Moss, Nat. Photon. **2**, 737 (2008).

[45] P. P. Absil, J. V. Hryniewicz, B. E. Little, P. S. Cho, R. A. Wilson, L. G. Joneckis, and P.-T. Ho, Opt. Lett. **25**, 554 (2000).

[46] Y. Dumeige and P. Feron, Phys. Rev. A **74**, 063804 (2006).

[47] J. S. Levy, M. A. Foster, A. L. Gaeta, and M. Lipson, Opt. Express **19**, 11415 (2011).

[48] K. Rivoire, S. Buckley, F. Hatami, and J. Vuckovic, Appl. Phys. Lett. **98**, 263113 (2011).

[49] S. Buckley, M. Radulaski, K. Biermann, and J. Vuckovic, arXiv:1308.6051v1.

[50] K. Rivoire, Z. Lin, F. Hatami, and J. Vuckovic, Appl. Phys. Lett. **97**, 043103 (2010).

[51] B. Kuyken, S. Clemmen, S. K. Selvaraja, W. Bogaerts, D. V. Thourhout, P. Emplit, S. Massar, G. Roelkens, and R. Baets, Opt. Lett. **36**, 552 (2011).

[52] T. Carmon and K. J. Vahala, Nature (London) **3**, 430 (2007).

[53] H. Fukuda, K. Yamada, T. Shoji, M. Takahashi, T. Tsuchizawa, T. Watanabe, J. Takahashi, and S. Itabashi, Opt. Express **13**, 4629 (2005).

[54] S. Reza, M. A. Foster, A. C. Turner, D. F. Geraghty, M. Lipson, and A. L. Gaeta, Nat. Photon. **2**, 35 (2008).

[55] I. Agha, M. Davanco, B. Thurston, and K. Srinivasan, Opt. Lett. **37**, 2997 (2012).

[56] P. Del'Haye, A. Schliesser, O. Arcizet, T. Wilken, R. Holzwarth, and T. J. Kippenberg, Nature (London) **450**, 1214 (2007).

[57] J. S. Levy, A. Gondarenko, M. A. Foster, A. C. Turner, A. L. Gaeta, and M. Lipson, Nat. Photon. **4**, 37 (2010).

[58] Y. Okawachi, K. Saha, J. S. Levy, Y. H. Wen, M. Lipson, and A. L. Gaeta, Opt. Lett. **36**, 3398 (2011).

[59] I. B. Burgess, A. W. Rodriguez, M. W. McCutecheon, J. Bravo-Abad, Y. Zhang, S. G. Johnson, and M. Loncar, Opt. Express **17**, 9241 (2009).

[60] Z.-F. Bi, A. W. Rodriguez, H. Hashemi, D. Duchesne, M. Loncar, K. Wang, and S. G. Johnson, Opt. Express **20**, 7 (2012).

[61] J. D. Joannopoulos, R. D. Meade, and J. N. Winn, *Photonic Crystals: Molding the Flow of Light* (Princeton University Press, Princeton, NJ, 1995).

[62] C. Sauvan, G. Lecamp, P. Lalanne, and J. P. Hugonin, Opt. Express **13**, 245 (2005).

[63] A. R. M. Zain, N. P. Johnson, M. Sorel, and R. M. DeLaRue, Opt. Express **16**, 12084 (2008).

[64] M. W. McCutcheon and M. Loncar, Opt. Express **16**, 19136 (2008).

[65] M. Notomi, E. Kuramochi, and H. Taniyama, Opt. Express **16**, 11095 (2008).

[66] Y. Zhang, M. W. McCutcheon, I. B. Burgess, and M. Loncar, Opt. Lett. **34**, 17 (2009).

[67] Q. Quan and M. Loncar, Opt. Express **19**, 18529 (2011).

[68] H. A. Haus, *Waves and Fields in Optoelectronics* (Prentice-Hall, Englewood Cliffs, NJ, 1984).

[69] V. S. Afraimovich and L. P. Shilnikov, *Strange Attractors and Quasiattractors in Nonlinear Dynamics and Turbulence* (Pitman, New York, 1983).

[70] L. Lugiato, C. Oldano, C. Fabre, E. Giacobino, and R. Horowicz, Il Nuovo Cimento D **10**, 959 (1988).

[71] C. Richy, K. I. Petsas, E. Giacobino, C. Fabre, and L. Lugiato, J. Opt. Soc. Am. B **12**, 456 (1995).

[72] S. H. Strogatz, *Nonlinear Dynamics and Chaos* (Westview, Boulder, CO, 1994).

[73] M. Tonouchi, Nat. Photon. **1**, 97 (2007).

[74] Y. S. Lee, T. Meade, V. Perlin, H. Winful, T. B. Norris, and A. Galvanauskas, Appl. Phys. Lett. **76**, 2505 (2000).

[75] K. L. Vodopyanov, M. M. Fejer, X. Xu, J. S. Harris, Y. S. Lee, W. C. Hurlbut, V. G. Kozlov, D. Bliss, and C. Lynch, Appl. Phys. Lett. **89**, 141119 (2006).

[76] A. Andornico, J. Claudon, J. M. Gerard, V. Berger, and G. Leo, Opt. Lett. **33**, 2416 (2008).

[77] J. Bravo-Abad, A. W. Rodriguez, J. D. Joannopoulos, P. T. Rakich, S. G. Johnson, and M. Soljacic, Appl. Phys. Lett. **96**, 101110 (2010).

[78] Q. Lin, J. Zhang, G. Piredda, R. W. Boyd, P. M. Fauchet, and G. P. Agrawal, Appl. Phys. Lett. **91**, 021111 (2007).

[79] J. D. Joannopoulos, S. G. Johnson, J. N. Winn, and R. D. Meade, *Photonic Crystals: Molding the Flow of Light*, 2nd ed. (Princeton University Press, Princeton, NJ, 2008).

[80] M. Palamaru and P. Lalanne, Appl. Phys. Lett. **78**, 1466 (2001).

[81] G.-H. Kim and Y.-H. Lee, Opt. Express **12**, 26 (2004).

[82] A. Faraon, E. Waks, D. Englund, I. Fushman, and J. Vuckovic, Appl. Phys. Lett. **90**, 073102 (2007).

[83] M. G. Banaee, A. G. Pattantyus-Abraham, M. W. McCutcheon, G. W. Rieger, and J. F. Young, Appl. Phys. Lett. **90**, 193106 (2007).

[84] P. E. Barclay, K. Srinivasan, and O. Painter, Opt. Express **13**, 801 (2005).

[85] P. B. Deotare, M. W. McCutcheon, I. W. Frank, M. Khan, and M. Loncar, Appl. Phys. Lett. **94**, 121106 (2009).

[86] T. K. Liang and H. K. Tsang, Appl. Phys. Lett. **84**, 2745 (2004).

[87] X. Yang and C. W. Wong, Opt. Express **15**, 4763 (2007).

[88] H. Rong, Y.-H. Kuo, A. Liu, M. Paniccia, and O. Cohen, Opt. Express **14**, 1182 (2006).

[89] X. Zeng and M. A. Popović, arXiv:1310.7078.

[90] J. R. Ong, R. Kumar, R. Aguinaldo, and S. Mookherjea, IEEE Photon. Tech. Lett. **25**, 17 (2013).

[91] K. Yamada, H. Fukuda, T. Tsuchizawa, T. Watanabe, T. Shoji, and S. Itabashi, IEEE Photon. Tech. Lett. **18**, 1046 (2006).

[92] A. C. Turner, M. A. Foster, A. L. Gaeta, and M. Lipson, Opt. Express **16**, 4881 (2008).

[93] E. Engin, D. Bonneau, C. M. Natarajan, A. S. Clark, M. G. Tanner, R. H. Hadfield, S. N. Dorenbos, V. Zwiller, K. Ohira, N. Suzuki *et al.*, Opt. Express **21**, 27826 (2013).